iScience

CellPress
OPEN ACCESS

Article

Second-order associative memory circuit hardware implemented by the evolution from battery-like capacitance to resistive switching memory

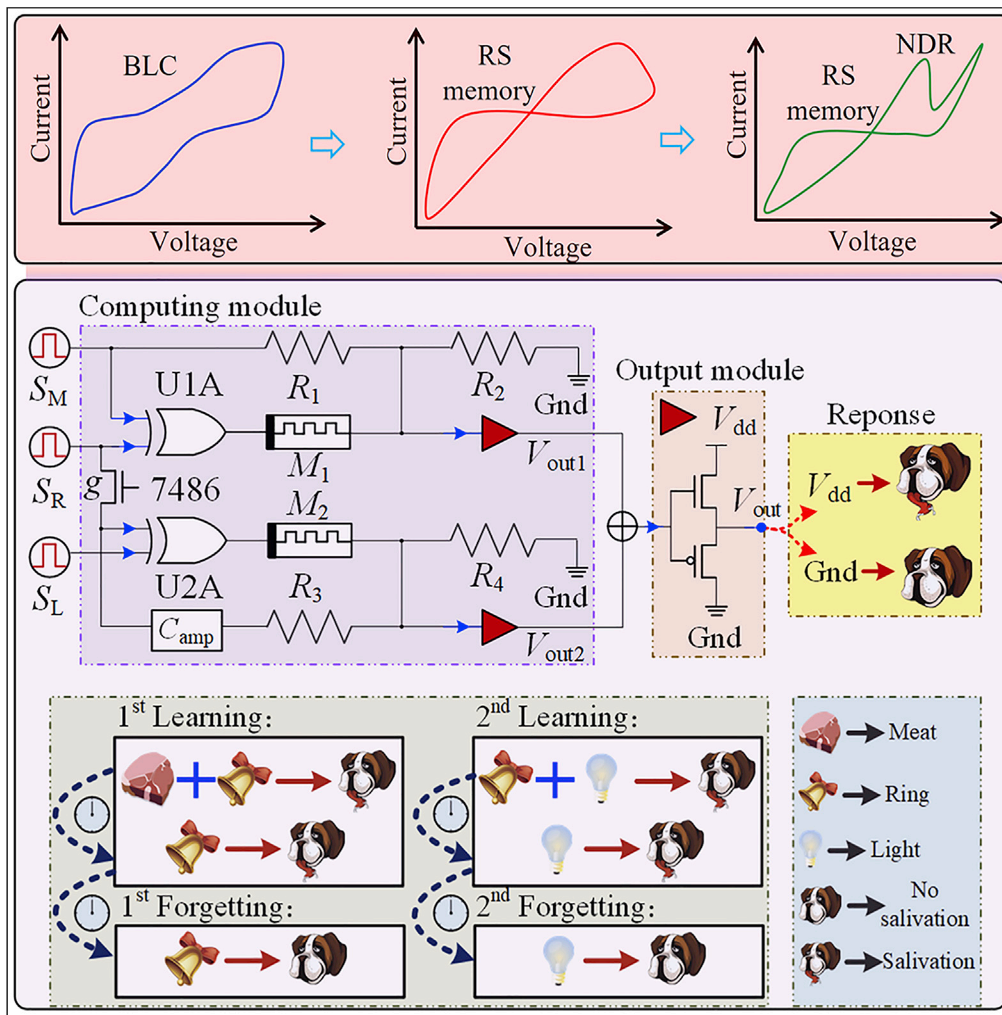

Guangdong Zhou, Xiaoye Ji, Jie Li, ..., Qunliang Song, Lidan Wang, Shukai Duan

zhougd@swu.edu.cn (G.Z.)
zhoufc@sustech.edu.cn (F.Z.)
bsun@swjtu.edu.cn (B.S.)
duansk@swu.edu.cn (S.D.)

Highlights

Evolution map of the memristor is extended by the negative differential resistance

Second-order associate memory circuit is full hardware implementation

Ion accumulation, migration, and formation of conduction paths are major reason

All evolution processes are verified by the FeO_x-based memristor

Zhou et al., iScience *25*, 105240
October 21, 2022 © 2022
https://doi.org/10.1016/j.isci.2022.105240

iScience

CellPress OPEN ACCESS

Article

Second-order associative memory circuit hardware implemented by the evolution from battery-like capacitance to resistive switching memory

Guangdong Zhou,[1,5,*] Xiaoye Ji,[2] Jie Li,[3] Feichi Zhou,[3,*] Zhekang Dong,[2] Bingtao Yan,[1] Bai Sun,[4,*] Wenhua Wang,[1] Xiaofang Hu,[1] Qunliang Song,[1] Lidan Wang,[1] and Shukai Duan[1,*]

SUMMARY

Memristor-based Pavlov associative memory circuit presented today only realizes the simple condition reflex process. The secondary condition reflex endows the simple condition reflex process with more bionic, but it is only demonstrated in design and involves the large number of redundant circuits. A FeO_x-based memristor exhibits an evolution process from battery-like capacitance (BLC) state to resistive switching (RS) memory as the *I-V* sweeping increase. The BLC is triggered by the active metal ion and hydroxide ion originated from water molecule splitting at different interfaces, while the RS memory behavior is dominated by the diffusion and migration of ion in the FeO_x switching function layer. The evolution processes share the nearly same biophysical mechanism with the second-order conditioning. It enables a hardware-implemented second-order associative memory circuit to be feasible and simple. This work provides a novel path to realize the associative memory circuit with the second-order conditioning at hardware level.

INTRODUCTION

Memristor, which is characterized by the nonvolatile resistance switching, has made great breakthrough in ultra-high data storage (Wang et al., 2020a, 2020b; Sun et al., 2021a, 2021b), circuit system (Kim et al., 2021; Wan et al., 2014), and neuromorphic computing because of its non-linearity, low-power consumption, and synaptic bionic (Li et al., 2020; Wang et al., 2019; Zhou et al., 2021; Martin et al., 2022).

Different applications require different types of memristor (Zhou et al., 2019a, 2019b, 2019c, 2019d; Ma et al., 2020). The digital-type memristor that is featured by high resistance ratio, fast switching speed, and long retention time is suitable for the ultra-high data storage and digital logic circuit, while the analog-type memristor, which is characterized by the high non-linearity, reliable nonvolatility, and multi-conductance states, is desirable for neuromorphic computing and associative memory circuit (Ma et al., 2020; Zhou et al., 2022; Zhang et al., 2020).

The ion dynamic process during the non-linear resistance change endows the memristor with unique merit to mimic the brain function. For instance, the in-sensor computing was realized using the coupling effect between photon and ion (Zhang et al., 2020; Wang et al., 2020a, 2020b; Mennel et al., 2020); the third-order nanocircuit element of the neuromorphic computing was developed by controlling the crystallization kinetic process (Zhou et al., 2018; Hu et al., 2021; Kumar et al., 2021); and the neuro-transistor could faithfully mimic the neurotransmitter release by the ion diffusion process (Wang et al., 2018). Utilizing the ion/electron accumulation, diffusion, and migration in the switching function layer, the RS evolution processes including the non-standard faradic capacitance (NFC), battery-like capacitance (BLC), and RS memory behavior were discovered in our previous work (Sun et al., 2019; Zhou et al., 2020; Sun et al., 2020a, 2020b; Sun et al., 2021a, 2021b). The ion/electron dynamic processes offer the unique route to the memristor to faithfully mimic the function of human brain, such as forgetting and learning, which are the core processes of associative memory (Ziegler et al., 2012; Bannur et al., 2022; Bannur and Kulkarni, 2020).

The learning and forgetting functions of the classical Pavlov associative memory were demonstrated in both digital and analog memristor (Bannur et al., 2019; Liu et al., 2016; Wang et al., 2018; Sun

[1]College of Artificial Intelligence, School of Materials and Energy, Southwest University, Chongqing 400715, PR China

[2]College of Electrical Engineering, Zhejiang University, Hangzhou 310027, PR China

[3]Shenzhen-Hong Kong College of Microelectronics, Southern University of Science and Technology, Shenzhen 518055, China

[4]Department of Mechanics and Mechatronics Engineering, Centre for Advanced Materials Joining, Waterloo Institute for Nanotechnology, University of Waterloo, Waterloo, ON N2L 3G1, Canada

[5]Lead contact

*Correspondence: zhougd@swu.edu.cn (G.Z.), zhoufc@sustech.edu.cn (F.Z.), bsun@swjtu.edu.cn (B.S.), duansk@swu.edu.cn (S.D.)

https://doi.org/10.1016/j.isci.2022.105240

This is an open access article under the CC BY-NC-ND license (http://creativecommons.org/licenses/by-nc-nd/4.0/).

et al., 2020a, 2020b). Memristor-based Pavlov associative memory circuit was designed to realize associative cognitive functions (Zhang and Zeng, 2021). In addition, the electron vision of Pavlov associative memory was realized in the AgInSbTe and Ag/HfO_x/ITO memristor (Li et al., 2015; Pei et al., 2020; Ji et al., 2021). After combining the merits of analog memristor, the full-function Pavlov associative circuits were developed (Wu et al., 2016; Yang et al., 2018; Wang et al., 2018). Importantly, the group of Hong stressed that the Pavlov associative memory with second-order conditioning, which included two types of learning and forgetting processes, exhibited high performance on image classification (Du et al., 2021). Both simulation and real memristor for the associative circuit, thus, have made milestone progress during past decades. However, the associative circuit presented today still suffers from the limitation in the complexity of circuit and physical realization, because the circuit design does not take the elaborate RS dynamics into account.

In this work, an elaborate RS dynamic involving the evolution process from the BLC to RS state is demonstrated in the FeO_x-based memristor. Utilizing the different interaction between ion and electron for the BLC and RS state, an associate memory circuit verified by Pavlov associative memory with second-order conditioning is realized at hardware level.

RESULTS AND DISCUSSION

The memristor with the structure of Ag/FeO_x/Fe-based alloy is prepared to examine the evolution of RS memory behavior, as shown in Figure 1A. The cross-section FE-SEM image illustrates the thickness of the FeO_x switching layer is ~300 nm (top side of the Figure 1A). The FE-SEM image exhibits that the FeO_x switching layer is composed by nanosheets. Each nanosheet has an average width of ~100 nm and an average thickness of ~5 nm (Figure 1B). The 1.7 Å of inter-planar spacing observed in the HR-TEM image is contributed by the lattice plane of [422] (Figure 1C). The lattice planes of [211], [220], [311], [222], [400], [422], [511], and [440] obtained from the XRD measurement are consistent with the feature of γ-Fe_2O_3 (JCPDS: 39-1346). Thus, the main component of the switching layer is Fe_2O_3 (Figure 1D). The non-defined 2θ diffraction peaks located at 51.77° and 65.59° are also detected, implying that the Fe_2O_3 nanosheet possibly contains another iron-based component. The binding energy of the core level of Fe 2p is 710.7 and 724.5 eV, resulting in a splitting energy of 13.8 eV between $2p_{3/2}$ and $2p_{1/2}$ (Figure 1E). The splitting energy of 13.8 eV is mainly contributed by the Fe-O bond in the Fe_2O_3. The binding energy of 529.8 eV for the O 1s core level is well agreed with the Fe-O bond in the Fe_2O_3 (Figure 1F). Based on the characterization and analysis, the function layer is composed of Fe_2O_3.

Evolution process of the memristive system, which contains the pure capacitance state, non-standard faraday capacitance, BLC, and RS state (Zhou et al., 2020; Sun et al., 2021a, 2021b), is schematically demonstrated in Figure 1G. To further examine the evolution process of the Ag/Fe_2O_3/Fe-based alloy memristor, the current-voltage (*I-V*) sweepings were operated. One can see that the memristor presents a stable BLC state ranging from 1st to 200th voltage sweeping (Figure 2A). The BLC state is featured by an obvious oxidation peak located at ~0.2 V and a reduction peak located at ~1.2 V. The redox peaks are weaking as the increase of the *I-V* sweeping from 300th to 500th and the current also presents an obvious increase from ~6 to ~30 μA (Figure 2B). It notes that the redox peaks nearly disappear when the *I-V* sweepings increase from 600th to 782th and the corresponding current reaches to the compliance current level (Figure 2C). Therefore, the redox process is possibly submerged by the increasing current. Entering $900^{th} \sim 903^{th}$ sweepings, the redox process is thoroughly suppressed by the high current, but a pinched *I-V* hysteresis is detected (Figure 2D). The observation of the pinched *I-V* hysteresis implies that the Ag/Fe_2O_3/Fe-based alloy presents the RS memory behavior (Sun et al., 2020a, 2020b; Zhou et al., 2019a, 2019b, 2019c, 2019d). The RS memory behavior is maintained during $905^{th} \sim 917^{th}$ *I-V* sweepings (Figure 2E). The RS memory becomes stable during the $990^{th} \sim 1000^{th}$ *I-V* sweepings (Figure 2F). It is worth noting that the negative differential resistance (NDR) effect is also detected during this range.

The Ag/Fe_2O_3/Fe-based alloy memristor has experienced three stages: i) BLC stage at very beginning state, ii) RS memory behavior, and iii) coexistence of the RS memory behavior and NDR effect. It notes that the BLC and NDR effect involve the ion/electron-based redox reaction process. To calculate the number of charge (Q) of redox process, the memristor is set to short-circuit once it reaches to the oxidation peak current density ($J_{p\text{-}oxi}$) or reduction peak current density ($J_{p\text{-}red}$). After integrating the area of discharge current versus time, the Q was obtained. The redox process was described by the *Randles-Sevcik* equation (Valov et al., 2011; Valov et al., 2013):

CellPress
OPEN ACCESS

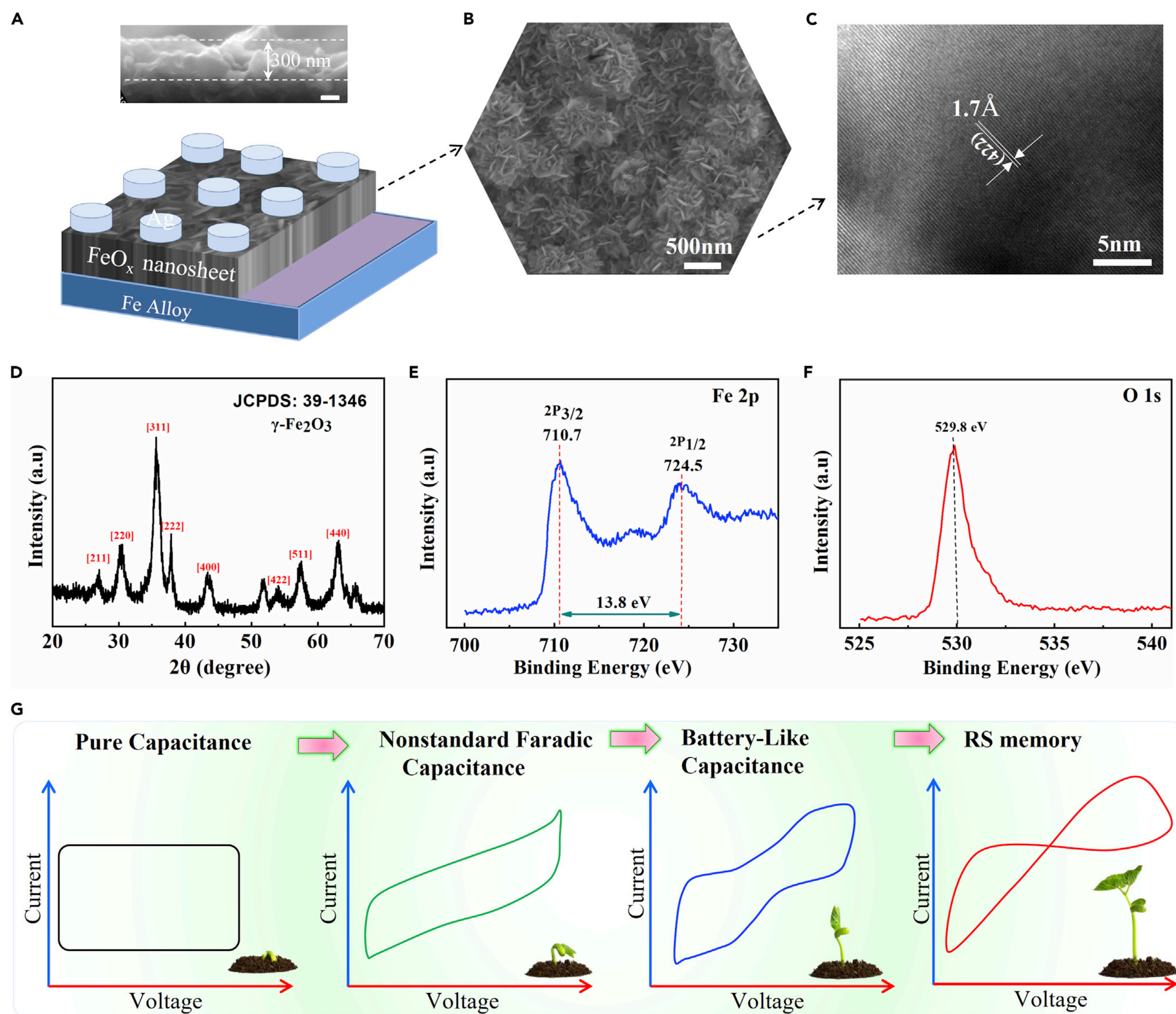

Figure 1. Memristor preparation and characterization

(A) Schematic diagram the memristor with the structure of Ag/Fe_2O_3/Fe-alloy. The FeO_x switching layer is about 300 nm, the scale bar is 100 nm.

(B) FE-SEM image of self-assembled FeO_x nanosheets.

(C) HR-TEM image of the FeO_x nanosheet characterized by the crystalline inter-planar spacing of 1.7 Å contributed by the lattice plane of [422] of the Fe_2O_3.

(D) The XRD pattern of the FeO_x film.

(E and F) XPS spectra of the core level of Fe 2p and O 1s.

(G) Schematical diagram the evolution process of memristor.

$$J_{p-\ redox} = 2.99\cdot 10^5 \cdot Z^{\frac{3}{2}} \cdot C_{redox} \cdot \sqrt{\alpha \vartheta D_{redox}} \quad \text{(Equation 1)}$$

where the J_p, Z, C_{redox}, α, ϑ, and D_{redox} denote the redox peak current value (A/cm^2), the number of electrons transferred during redox process, ions concentration (mol/cm^3), charge transfer coefficient, bias voltage scan rate, and ions diffusion coefficient (cm^2/s), respectively. The $J_{p\text{-}oxi}$ and $J_{p\text{-}red}$ can be given by integration area of discharge curve. At very initial stage, the active Ag electrode is oxidized to Ag^+, thus the number of transferred electrons in oxidation process is one (Z = 1). The charge transfer coefficient of α is ~0.5 and the bias voltage is 500 mV/s. In the Equation 1, the D_{redox} is given by the *Nernst-Einstein* relation (Valov et al., 2013).

$$\mu_{redox} = \frac{D_{redox} Ze}{K_B T} \quad \text{(Equation 2)}$$

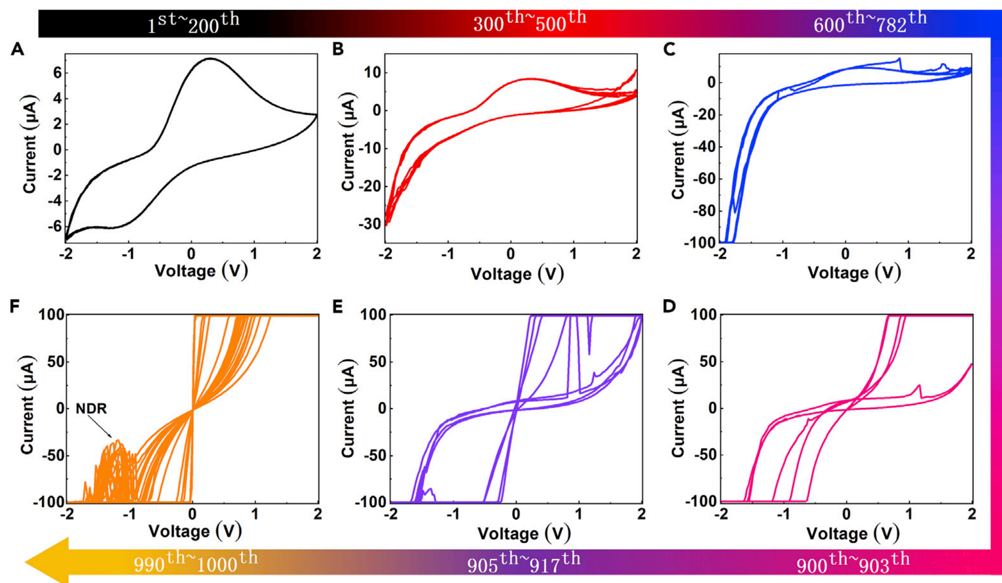

Figure 2. The converter from battery-like capacitance state to resistive switching (RS) behavior triggered by the cycling endurance

(A) Redox-based capacitance behavior during 200 *I-V* sweepings.

(B) The degraded redox-based capacitance behavior during the 300th~500th *I-V* sweepings.

(C) The degraded redox-based capacitance behavior becomes very weaken during the 600th ~782th *I-V* sweepings.

(D and E) Evolution from capacitance state to RS memory behavior.

(F) Coexistence of the negative differential resistance and RS memory behavior.

The μ_{redox}, K_B, and T are the ion mobility (cm^2/Vs), boltzman constant, and temperature, respectively. Here, the laboratory temperature is 27°C (T = 300 K) and K_B is 1.38×10^{-23} J/K. According to the Q_{redox} obtained from the integration of discharge versus time evolution, the C_{redox} can be calculated from the Equations 1 and 2. Therefore, the ion concentration of C_{redox} versus both D_{redox} and μ_{redox} can be given for the evolution process from BLC stage to RS memory behavior.

To the BLC stage, the peak current density of the $J_{p\text{-}oxi}$ (1.36×10^{-4}) and $J_{p\text{-}red}$ ($1.1 \times 10^{-4} A/cm^2$) is calculated by the corresponding peak current (inset of the Figure 3A) and the area of the top electrode (πr^2). After integrating the area of the discharge current versus time curve (Figures 3B and 3C), the Q_{oxi} (1.28×10^{-5} C) and Q_{red} (3.9×10^{-6} C) are obtained. The ion concentration of C_{oxi} (0.13 mol/cm^3) and C_{red} (0.012 mol/cm^3) is further calculated according to the transfer charge of the redox process. According to the Equation 1, the ions diffusion coefficient for the oxidation process is 4.89×10^{-17} cm^2/s (D_{oxi}), while the reduction process is 3.76×10^{-15} cm^2/s (D_{red}). From the Equation 2, the corresponding ion mobility is 1.73×10^{-15} cm^2/Vs and 1.44×10^{-13} cm^2/Vs for the oxidation (μ_{oxi}) and reduction (μ_{red}) process, respectively.

Entering the RS memory stage, the corresponding charge is obtained from the integration (Figures 3D and 3E). Comparing with the BLC stage, the C_{red} and C_{oxi} for the RS memory stage increase to 0.42 and 4.05 mol/cm^3, respectively. It will lead to the decrease of D_{redox} and μ_{redox} (Figure 3F). In particular, the μ_{oxi} is 3.98×10^{-16} cm^2/Vs and the D_{red} is 2.64×10^{-16} cm^2/s, which decreases one order of magnitude compared with BLC stage. The calculation demonstrates that i) the Ag/Fe_2O_3/Fe-based alloy with a low ion concentration at the BLC stage, but the ion holds a high mobility and diffusion; ii) entering the RS memory stage, the ion concentration sharply increases, but the mobility and diffusion are weakened. It notes that the C_{oxi} is higher than C_{red} for both BLC stage and RS memory behavior. Considering the oxidation reaction, the ionized Ag is described as following (Wan et al., 2019; Wan et al., 2020; Zhou et al., 2019a, 2019b, 2019c, 2019d; Yan et al., 2022):

$$Ag \rightleftharpoons Ag^{+} + e \quad \text{(Equation 3)}$$

According to Equation 3, the Ag electrode is ionized to be Ag^+, and then electric-field driven diffuses into the Fe_2O_3 layer. In addition, the oxygen vacancy (V_0) of the Fe_2O_3 is sensitive to water molecule. According

CellPress
OPEN ACCESS

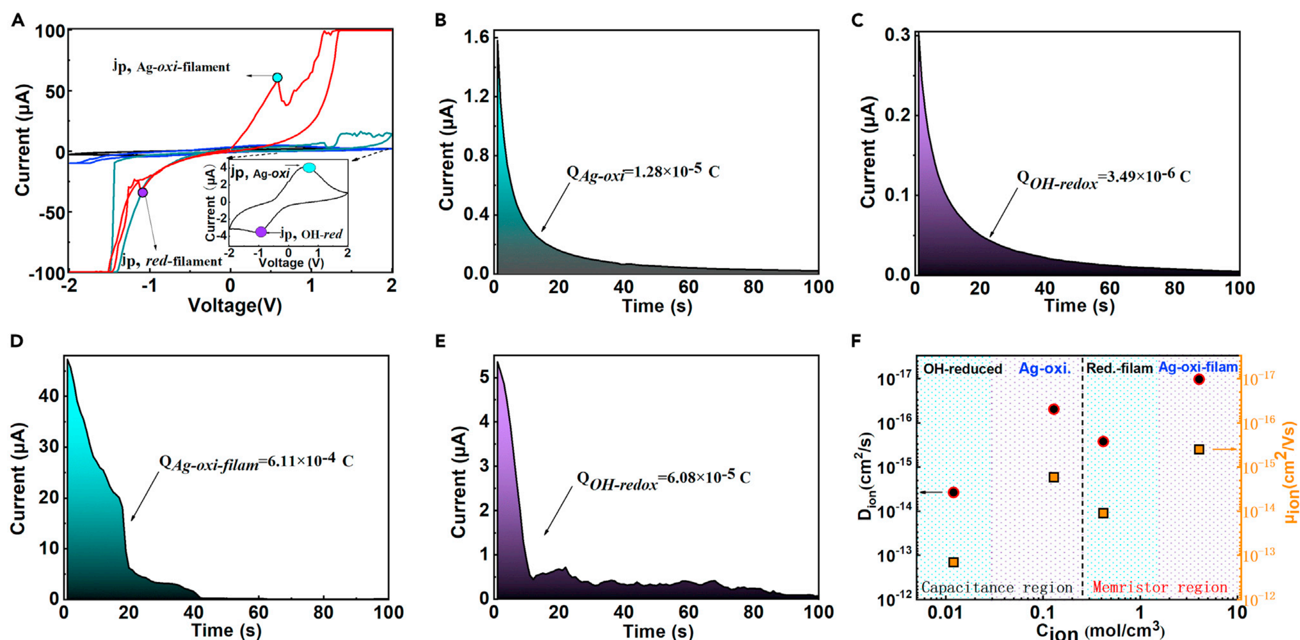

Figure 3. Ion concentration during the evolution process

(A) Evolution from the redox-based capacitance phase to the RS memory phase.

(B)–(E) Current versus time under short circuit for the memristor at different current peaks.

(F) Ion concentration versus migration rate and ions diffusion coefficients.

to the half-cell theory, the reduction reaction occurs at the counter electrode. Therefore, the redox reaction between water and Fe_2O_3 film is described as following (Yan et al., 2022; Liao et al., 2022; Messerschmitt et al., 2015):

$$H_2O + O_0^{\times} + V_0 \rightleftharpoons 2OH^- \quad \text{(Equation 4)}$$

where the $O_0^{\times}$ and V_0 denote the oxygen in lattice and oxygen vacancies, respectively. According to Equations 3 and 4, the current increases because the electron/ion diffusion and migration is enhanced, which is described by (Valov et al., 2013; Zhou et al., 2018):

$$\sigma = q\eta_{h^{\cdot}} c_{h^{\cdot}} + q\eta_{e'} c_{e'} + 2q\eta_{V_O^{\cdot\cdot}} c_{V_O^{\cdot\cdot}} + q\eta_{OH_O} c_{OH_O} \quad \text{(Equation 5)}$$

where the σ, q, c, μ, h, e, $V_O^{\cdot\cdot}$, and $OH_o^{\cdot}$ denote the electric conductivity, elemental charge, ions concentration, ions mobility, holes, electrons, oxygen vacancy, and proton bound to oxygen in the metal oxide, respectively.

Therefore, the C_{oxi} and C_{red} are respectively contributed by the Ag^+ and OH^- for both BLC stage and RS memory behavior. According to our previous studies, the evolution process was dominated by ion/electron accumulation at interface, reaction, and migration (Zhou et al., 2018, 2019a, 2019b, 2019c, 2019d). In other words, if the accumulation, reaction, and migration orderly happen under external stimulation, the evolution processes will happen regardless of the type of stimulations. To further verify this assumption, the *I-V* sweepings are measured under different moisture level because the water splitting on the surface can accelerate the evolution. Being similar with our previous studies (Zhou et al., 2019a, 2019b, 2019c, 2019d, 2020; Sun et al., 2020a, 2020b), the evolution processes are expectedly observed (Figure 4A). It notes that the similar evolution processes are observed under the voltage sweepings and high relative humidity. Therefore, the evolution processes for the memristive system are verified. To investigate the stability of the evolution process, resistance states for the BLC and RS are investigated. One can see that the transition state between the BLC and RS memory stage exhibits slightly volatile (Figure 4B). It stresses that the FeO_x-based memristor is nonvolatility and is modulated by compliance current after entering the RS memory and the coexistence stage (Figure 4C).

Based on above results and analysis, the evolution process can be comprehended. At very beginning stage, the Ag^+ and OH^- ion respectively distributes at the interface of Ag/FeO_x and FeO_x/Fe-alloy, resulting in the

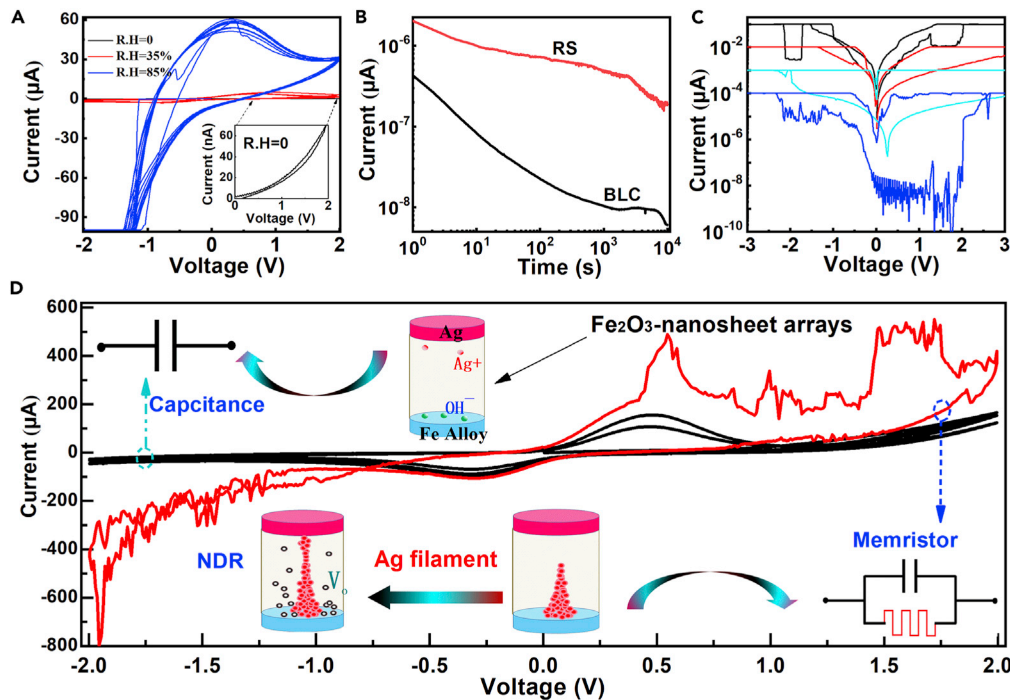

Figure 4. Physical mechanism for the evolutions

(A) The memristor shows the evolution process from the BLC, RS to NDR as the relative humidity increasing from 0% to 85%.

(B) The retention time measurement of the transition state between BLC and RS stage.

(C) The RS memory behavior is similar with most of memristive devices modulated by the compliance current once our memristor complicated the evolution process.

(D) Physicochemical dynamic process for the evolution RS memory behaviors. Under ultra-low bias voltage, the device exhibits the capacitance state due to the interface ions. A typical RS behavior is triggered by increasing voltage sweepings.

memristor exhibiting capacitance effect. The increase of ion concentration provides enough ions to diffuse and migrate in the switching layer, and finally forms a conduction filament, which directly leads to the memristor entering the RS memory behavior. The oxygen vacancy at surface ($V_{o\text{-}sur}$) and subsurface ($V_{o\text{-}sub}$) not only facilitates the water split to generate OH^- but also penetrates the switching layer to form nanofilament. In this case, the three types of mechanisms including the Ag filament, OH^-, and V_o conduction path lead to a coexistence of the RS memory behavior and NDR effect (Figure 4D).

According to the electron/ion dynamic, a second-order associative circuit that verified by the Pavlov associative memory is proposed. A flexible compact model is proposed to explore the dynamics in simulation. The simulation includes two current sources (G_m and G_x), and the 1F capacitor (C_x). The model is connected as the circuit schematic, in which the terminals plus and minus denote the top and bottom electrode of memristor. Notably, at the device level, 1F capacitance may be unrealistic; while at the model level, the 1F capacitor makes the circuit structure and mathematical expression easier and simpler. According to the equivalent circuit, the relationship between current and voltage is described as following:

$$i_{Gm}(t) = \begin{cases} a_1 x(t)^{n_1} v(t)^{b_1} + a_2\left(1 - x(t)^{n_2}\right)\left(1 - e^{-m_1 v(t)}\right), & v(t) \geq 0 \\ a_3 x(t)^{n_3} v(t)^{b_2} + a_4\left(1 - x(t)^{n_4}\right)\left(1 - e^{-m_2 v(t)}\right), & v(t) < 0 \end{cases} \quad \text{(Equation 6)}$$

where $v(t)$ denotes the applied voltage, $i_{Gm}(t)$ denotes the current passing through the memristor, a_1, a_2, a_3, a_4, b_1, b_2, n_1, n_2, n_3, n_4, m_1, and m_2 are the fitting parameters of the model. The *I-V* response curve of a mathematical model can approximate the actual physical model. The $a_1x(t)^{n1}$ and $a_3x(t)^{n3}$ terms are used to stimulate the dynamics of the $k\gamma/(\gamma+1)$ term in the space-charge limited current mechanism. The a_2 $(1\text{-}x(t)^{n2})(1\text{-}e^{-m1v(t)})$ and a_4 $(1\text{-}x(t)^{n4})(1\text{-}e^{-m2v(t)})$ terms are used to represent the Schottky tunneling current. The $x(t)$ denotes the state variable for characterizing the conductivity of the device, where $x \in [0,1]$. The

CellPress
OPEN ACCESS

value of $x(t)$ is derived by integrating the current $i_{Gx}(t)$ over time through capacitor C_x in the equivalent circuit.

The change in the state variable is mathematically expressed as:

$$i_{Gx}(t) = \frac{dx}{dt} = \begin{cases} \alpha_1\left(e^{\beta_1 v(t)} - e^{-\beta_2 v(t)}\right)f_{off}(x), v(t) > 0 \\ \alpha_2\left(e^{\beta_3 v(t)} - e^{-\beta_4 v(t)}\right)f_{on}(x), v(t) \le 0 \end{cases} \quad \text{(Equation 7)}$$

where α_1 and α_2 are the fitting parameters. The β_1, β_2, β_3, and β_4 denote the voltage control parameter. The $f_{off}(x)$ and $f_{on}(x)$ as the window functions are employed to ensure the state variable $x(t)$ at the range of [0, 1]. They are described as following:

$$\begin{cases} f_{off}(x) = \exp\left[-\exp\left(\frac{x - a_{off}}{w_c}\right)\right], v(t) > 0 \\ f_{on}(x) = \exp\left[-\exp\left(\frac{a_{on} - x}{w_c}\right)\right], v(t) \le 0 \end{cases} \quad \text{(Equation 8)}$$

where w_c, a_{off}, and a_{on} are the fitting parameters.

Based on above theoretical description and mathematical derivation, the proposed memristor-based Spice model is obtained, in which the detail sub-circuit description is shown in Table S1. The gradient descent and minimized the relative error function value were used to measure the fit between the real memristor and circuit model. Here, the error function is selected as the relative root mean squared error (RRMSE):

$$E_{rrms} = \sqrt{\frac{1}{N}\cdot\left(\frac{\sum_{k=1}^{N}\left(V_k - V_{ref,k}\right)^2}{V_{ref}^2} + \frac{\sum_{k=1}^{N}\left(I_k - I_{ref,k}\right)^2}{I_{ref}^2}\right)} \quad \text{(Equation 9)}$$

where N is the total number of samples, and V_k and $V_{ref,k}$ denote the k_{th} voltage applied to the terminals of the memristor and the circuit model, respectively. The I_k and $I_{ref,k}$ represent the k_{th} current through the memristor and circuit model, respectively. The V_{ref} and I_{ref} are the Euclidean norms of voltage and current of the circuit model, respectively.

The corresponding fitting result and parameter setting are shown in Figure 5A, where the solid spheres and solid lines represent the experimental data and model data, respectively. The whale optimization algorithm is used to obtain all the parameters in Equations 6, 7, and 8. The initial value of state variable $x(t)$ is 0. Figure 5B illustrates the simulation results of the memristor after 300th switching cycles. When the state variable $x(t)$ approaches to zero, the memristor exhibits a BLC behavior. After obtaining the RRMSE from the theoretical fitting, a 0.106% is obtained for the experimental data. When the switching cycles increase to 600th and 782th, the state variable $x(t)$ gradually increases as the maximum current increases to 12 μA. In this case, a typical RS behavior is observed in positive voltage region (Figure 5C). In this region, the fitted curve is well matched with the target data and the corresponding RRMSE is 0.227%. The coexistence of NDR and RS memory behavior is observed when the $x(t)$ approaches to one (Figure 5D). By comparison, the peak current value of the memristor increases from 12 to 100 μA, and the RRMSE is 0.514%.

The second-order Pavlov conditioning behavior emerges along with the establishment of the classic Pavlov conditioned reflex (Figure 6A). The fabricated memristor exhibits an impressive evolution process from the BLC state to RS state, which shares the nearly same biophysical mechanism with the second-order conditioning. It enables a fully hardware-implemented second-order associative memory circuit to be feasible and simple (Figure 6B). The U1A and U2A are two XOR logic gates. The C_{amp} means the voltage amplification circuit with the magnification A of 7. The M_1 and M_2 are the two memristor cells in BLC state and RS state, respectively.

The initial memristance of 10^6 (R_{H1}) and 10^4 (R_{L1}) is selected in BLC state, respectively. The R_1, R_2, R_3, and R_4 are four fixed resistors, satisfying $R_1 = R_3 = R_{L2} \ll R_2 = R_4 \ll R_{H1}$. Meat signal S_M, ring signal S_R, and light signal S_L are three input voltages with two different states, which can be respectively represented by the

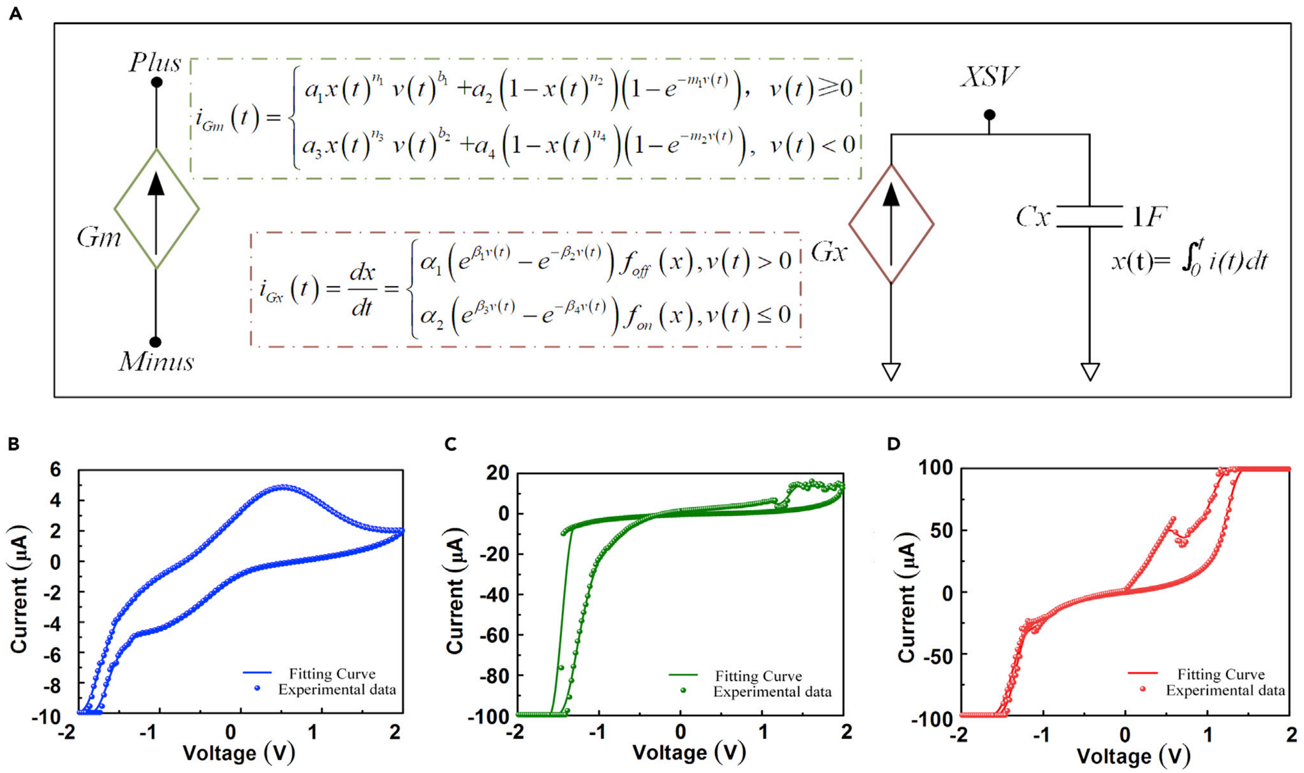

Figure 5. Equivalent circuit and simulations for the evolution from capacitance state to RS behaviors

The related programming code shows in Table S1.

(A) The equivalent circuit model for the Ag/Fe_2O_3/Fe-alloy memristor.

(B–D) Simulation (line) versus experimental results (dot): (B) the capacitance state, (C) the typical RS behavior, and (D) the coexistence of the negative differential resistance and RS memory behavior.

high-level state V_H (2 V) and the low-level state V_L (0 V). The transistor plays the role of switch with a control voltage g. The output voltage V_{out} depends on the sum of V_{out1} and V_{out2}. The output voltage V_{out} = 2 V (V_{dd}) indicates the dog secretes saliva. Contrarily, the dog does not secrete saliva when the output voltage V_{out} = 0 V(GND). To further demonstrate the merit of the proposed second-order associative memory circuit, simulation and analysis are conducted. One can see that the proposed circuit not only realizes the classical Pavlov conditioned reflex but also has the second-order conditioning behavior, in which the first conditioned reflex is realized by the BLC state, and the second conditioned reflex is realized by the RS state (Figure 6C).

Classic Pavlov conditioned reflex is divided into three phases: the premise phase, first learning phase, and first forgetting phase. To simulate these three phases, the control voltage g (green line) and light signal S_L (black line) remain in low-level state V_L. During the premise phase (0–200 ms), the meat signal S_M (red line) and ring signal S_R (blue line) are respectively assigned to V_H and V_L. In this case, the output voltage $V_{out} = V_{dd} = V_H$ implies the dog secretes saliva. Contrarily, the S_M and S_R are respectively assigned to V_L and V_H; the output voltage obeys the V_{out} = GND = V_L, indicating the dog does not secrete saliva. M_1 (orange line) and M_2 (cyan line) are maintained in the BLC state and RS state, respectively. During the first learning phase (200–700 ms), the S_M and S_R are assigned to V_H, implying that the meat and ring are both provided to the dog. M_1 quickly switches from BLC state to RS state and the output $V_{out} = V_{dd} = V_H$, which means that the dog secretes saliva. Once the S_M is removed, the first forgetting phase will start along with the entire second-order Pavlov conditioning.

Similarly, the second-order Pavlov conditioning is also divided into three phases: the premise phase, second learning phase, and second forgetting phase (Figure 6D). To simulate these three phases, the control signal g and S_M are respectively operated to the V_H and V_L, implying that the meat is removed. During the

CellPress
OPEN ACCESS

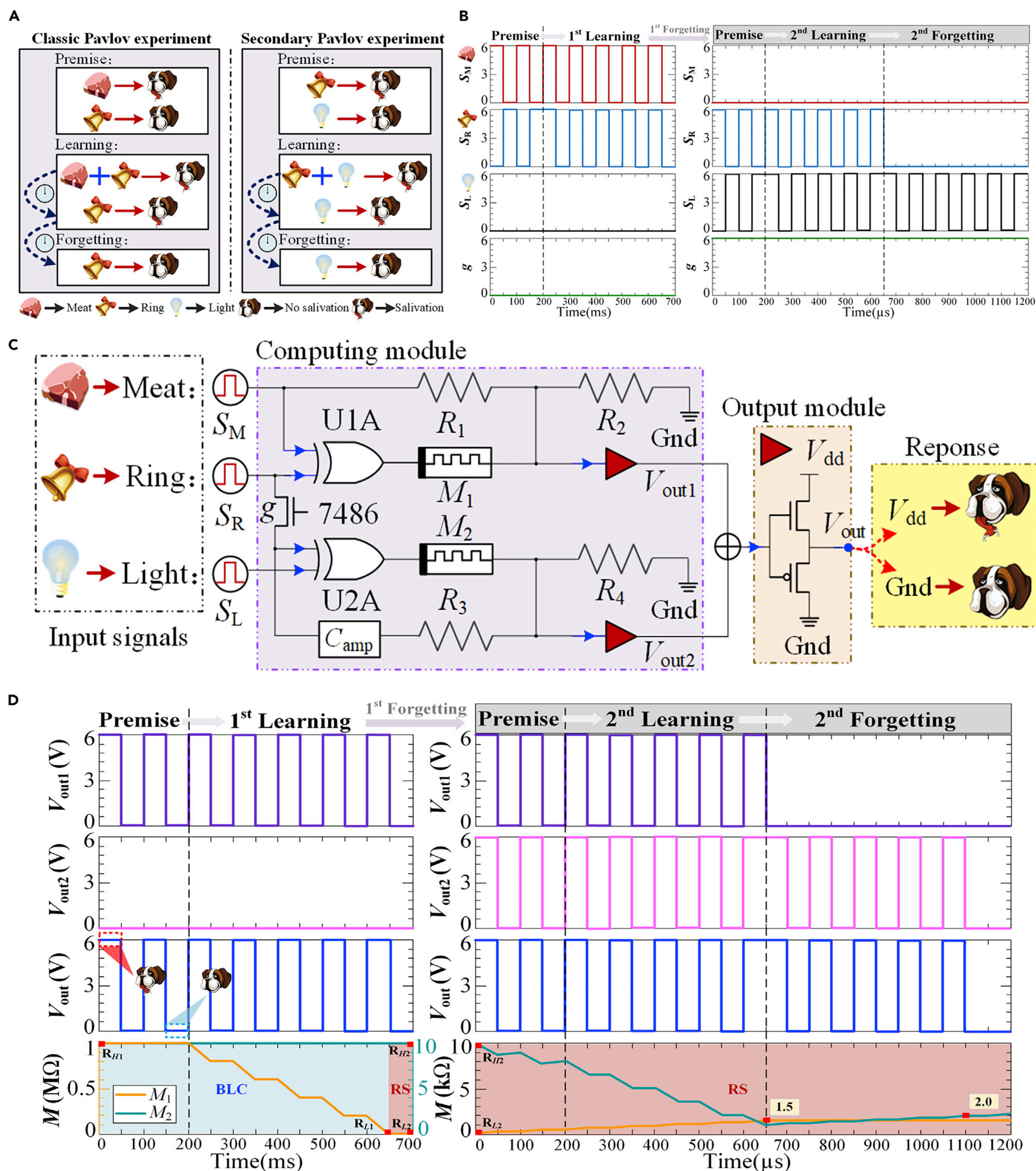

Figure 6. A fully hardware-implemented second-order associative memory circuit for neuromorphic computing

(A) The collected information of classic/secondary Pavlov conditioned reflex experiments.

(B) Input signals of the proposed second-order associative memory circuit.

(C) The Ag/Fe_2O_3/Fe-alloy memristor-based second-order associative memory circuit.

(D) Outputs of the proposed second-order associative memory circuit.

premise phase (0–200 μs), the S_R and light signal (S_L) are operated to V_H and V_L, respectively. In this case, the output voltage satisfies the V_{out} = V_{dd} = V_H; thus, the dog secretes saliva. Contrarily, the S_R and S_L are respectively assigned to V_L and V_H. In this case, the output voltage V_{out} = GND = V_L implies the dog does not secrete saliva. During the second learning phase (200–650 μs), the S_R and S_L are assigned to V_H, indicating that the ring and light are both provided to the dog. Here, the M_1 and M_2 are 0.5 and 7.6 kΩ, respectively. The dog secretes saliva (V_{out} = V_{dd} = V_H) and the associative memory between the ring and light is established. During the second forgetting phase (650–1,200 μs), the S_R and S_L are respectively operated to V_L and V_H. The M_1 remains unchanged at 1.5 kΩ, while M_2 increases to 2 kΩ. The V_{out} decreases from V_H to V_L, indicating the dog does not secrete saliva. In other words, the second-order conditioning established before is disappeared.

Conclusion

Memristor evolution involving the BLC stage and RS memory behavior is systemically examined. The electron/ion accumulated at interface and the concomitant redox reaction is responsible for the BLC stage. Electron/ion accumulation, migration, and diffusion are enhanced by the increasing *I-V* sweepings. The RS memory behavior and coexistence of NDR are ascribed to the growth of the different types of conduction paths. The corresponding dynamics in simulation are also explored by constructing a flexible compact model of the developed memristor. Furthermore, a memristor-based second-order associative memory circuit with second-order conditioning is designed and implemented, which opens a novel path for the deep integration of physical memristors into neuromorphic computing systems.

Limitations of the study

This work is mainly focused on the physical mechanism of the memristor and related the second-order associative memory circuit with second-order conditioning with the evolution process (From BLC to the coexistence of NDR and RS memory behavior). The circuit model and simulation only represent the specific I-V curve; thus, it is limited in terms of the cycle-to-cycle stability. In addition, the evolution can be triggered by the electric field, or testing environment, these factors have not considered in the physical models. The charge releasing is roughly estimated by the releasing charge by the short circuit. Large number of peripheral circuits and ideal capacitors are used during the simulations. Large-scale memristor array integration and parameter control are required to further realize the complex function and application in the future.

STAR★METHODS

Detailed methods are provided in the online version of this paper and include the following:

- KEY RESOURCES TABLE
- RESOURCE AVAILABILITY
  - Lead contact
  - Materials availability
  - Data and code availability
- EXPERIMENTAL MODEL AND SUBJECT DETAILS
- METHOD DETAILS
  - Measurements and instruments
  - Device fabrication and characterization
  - Circuit model and soft simulation
- QUANTIFICATION AND STATISTICAL ANALYSIS
- ADDITIONAL RESOURCES

SUPPLEMENTAL INFORMATION

Supplemental information can be found online at https://doi.org/10.1016/j.isci.2022.105240.

ACKNOWLEDGMENTS

This work was supported by the Fundamental Research Funds for the Central Universities (Grant No. SWU020019), Natural Science Foundation of Chongqing (Grant No. cstc2020jcyj-msxm X0648), Natural Science Foundation of Guizhou Province ([2020]1Y024).

AUTHOR CONTRIBUTIONS

G.Z. and X.J. conducted all experiments and data analysis. J.L. conducted the mechanism fitting results. F.Z., S.K.D., B.S., X.J., and G.D.Z. proposed the conception. B.Y., W.W., L.W., X.H., and Z.D. conducted the material characterization. Q.L.S. gave key guidance. G.Z., X.J., and J.L. equally contribute to this work.

DECLARATION OF INTERESTS

The authors declare no competing interests.

Received: May 31, 2022
Revised: August 29, 2022
Accepted: September 27, 2022
Published: October 21, 2022

REFERENCES

Bannur, B., Yadav, B., and Kulkarni, G.U. (2022). Second-order conditioning emulated in an artificial synaptic network. ACS Appl. Electron. Mater. *4*, 1552–1557. https://doi.org/10.1021/acsaelm.1c01237.

Bannur, B., and Kulkarni, G.U. (2020). On synapse intelligence emulated in a self-formed artificial synaptic network. Mater. Horiz. *7*, 2970–2977. https://doi.org/10.1039/D0MH01037E.

Bannur, B., Harish, K.N., Rao, K.D.M., and Kulkarni, G.U. (2019). Solution-based fast fabrication of a high-performance unlimited area Au nanostructure/Si heterojunction photodetector. ACS Appl. Electron. Mater. *1*, 577–584. https://doi.org/10.1021/acsaelm.9b00031.

Du, S., Deng, Q., Hong, Q., and Wang, C. (2021). A memristor-based circuit design of Pavlov associative memory with secondary conditional reflex and its application. Neurocomputing *463*, 341–354. https://doi.org/10.1016/j.neucom.2021.08.045.

Hu, X., Wang, W., Sun, B., Wang, Y., Li, J., and Zhou, G. (2021). Refining the negative differential resistance effect in a TiOx-based memristor. J. Phys. Chem. Lett. *12*, 5377–5383. https://doi.org/10.1021/acs.jpclett.1c01420.

Ji, X., Paulsen, B.D., Chik, G.K.K., Wu, R., Yin, Y., Chan, P.K.L., and Rivnay, J. (2021). Mimicking associative learning using an ion-trapping non-volatile synaptic organic electrochemical transistor. Nat. Commun. *12*, 2480. https://doi.org/10.1038/s41467-021-22680-5.

Kim, S.J., Kim, S.B., and Jang, H.W. (2021). Competing memristors for brain-inspired computing. iScience *24*, 101889. https://doi.org/10.1016/j.isci.2020.101889.

Kumar, S., Williams, R.S., and Wang, Z. (2021). Third-order nanocircuit elements for neuromorphic engineering. Nature *585*, 518–523. https://doi.org/10.1038/s41586-020-2735-5.

Li, Y., Xu, L., Zhong, Y.P., Zhou, Y.X., Zhong, S.J., Hu, Y.Z., Chua, L.O., and Miao, X.S. (2015). Memristors: associative learning with temporal contiguity in a memristive circuit for large-scale neuromorphic networks. Adv. Electron. Mater. *1*, 1500125. https://doi.org/10.1002/aelm.201570026.

Li, Y., Lu, J., Shang, D., Liu, Q., Wu, S., Wu, Z., Zhang, X., Yang, J., Wang, Z., Lv, H., and Liu, M. (2020). Oxide-based electrolyte-gated transistors for spatiotemporal information processing. Adv. Mater. *32*, e2003018. https://doi.org/10.1002/adma.202003018.

Liao, C., Hu, X., Liu, X., Sun, B., and Zhou, G. (2022). Self-selective analogue FeOx-based memristor induced by the electron transport in the defect energy level. Appl. Phys. Lett. *121*, 123505. https://doi.org/10.1063/5.0102076.

Liu, X., Zeng, Z., and Wen, S. (2016). Implementation of memristive neural network with full-function Pavlov associative memory. IEEE Trans. Circ. Syst. I *63*, 1454–1463. https://doi.org/10.1109/TCSI.2016.2570819.

Martin, E., Ernoult, M., Laydevant, J., Li, S., Querlioz, D., Petrisor, T., and Grollier, J. (2022). Eqspike: spike-driven equilibrium propagation for neuromorphic implementations. iScience *24*, 102222. https://doi.org/10.1016/j.isci.2021.102222.

Ma, Q.Y., Mao, J.Y., Ren, Y., Yang, X., Zhou, Y., and Han, S.T. (2020). Leaky integrate-and-fire neurons based on perovskite memristor for spiking neural networks. Nano Energy *74*, 104828. https://doi.org/10.1016/j.nanoen.2020.104828.

Mennel, L., Symonowicz, J., Wachter, S., Polyushkin, D.K., Molina-Mendoza, A.J., and Mueller, T. (2020). Ultrafast machine vision with 2D material neural network image sensors. Nature *579*, 62–66. https://doi.org/10.1038/s41586-020-2038-x.

Messerschmitt, F., Kubicek, M., and Rupp, J.L.M. (2015). How does moisture affect the physical property of memristance for anionic-electronic resistive switching memories? Adv. Funct. Mater. *25*, 5117–5125. https://doi.org/10.1002/adfm.201501517.

Pei, Y., Zhou, Z., Chen, A.P., Chen, J., and Yan, X. (2020). A carbon-based memristor design for associative learning activities and neuromorphic computing. Nanoscale *12*, 13531–13539. https://doi.org/10.1039/D0NR02894K.

Sun, B., Chen, Y., Xiao, M., Zhou, G., Ranjan, S., Hou, W., Zhu, X., Zhao, Y., Redfern, S.A.T., and Zhou, Y.N. (2019). A unified capacitive-coupled memristive model for the nonpinched current-voltage hysteresis loop. Nano Lett. *19*, 6461–6465. https://doi.org/10.1021/acs.nanolett.9b02683.

Sun, B., Xiao, M., Zhou, G., Ren, Z., Zhou, Y., and Wu, Y. (2020a). Non-zero-crossing current-voltage hysteresis behavior in memristive system. Mater. Today Adv. *6*, 100056. https://doi.org/10.1016/j.mtadv.2020.100056.

Sun, J., Han, G., Zeng, Z., and Wang, Y. (2020b). Memristor-based neural network circuit of full-function Pavlov associative memory with time delay and variable learning rate. IEEE Trans. Cybern. *50*, 2935–2945. https://doi.org/10.1109/TCYB.2019.2951520.

Sun, L., Wang, Z., Jiang, J., Kim, Y., Joo, B., Zheng, S., Lee, S., Yu, W.J., Kong, B.S., and Yang, H. (2021a). In-sensor reservoir computing for language learning via two dimensional memristors. Sci. Adv. *7*, eabg1455. https://doi.org/10.1126/sciadv.abg1455.

Sun, B., Guo, T., Zhou, G., Ranjan, S., Jiao, Y., Wei, L., Zhou, Y.N., and Wu, Y.A. (2021b). Synaptic devices based neuromorphic computing applications in artificial intelligence. Mater. Today Phys. *18*, 100393. https://doi.org/10.1016/j.mtphys.2021.100393.

Valov, I., Waser, R., Jameson, J.R., and Kozicki, M.N. (2011). Electrochemical metallization memories-fundamentals, applications, prospects. Nanotechnology *22*, 254003. https://doi.org/10.1088/0957-4484/22/25/254003.

Valov, I., Linn, E., Tappertzhofen, S., Schmelzer, S., van den Hurk, J., Lentz, F., and Waser, R. (2013). Nanobatteries in redox-based resistive switches require extension of memristor theory. Nat. Commun. *4*, 1771. https://doi.org/10.1038/ncomms2784.

Wan, C., Zhou, J., Shi, Y., and Wan, Q. (2014). Classical conditioning mimicked in junctionless IZO electric-double-layer thin-film transistors. IEEE Electron. Device Lett. *35*, 414–416. https://doi.org/10.1109/LED.2014.2299796.

Wan, C., Cai, P., Wang, M., Qian, Y., Huang, W., and Chen, X. (2019). Artificial sensory memory. Adv. Mater. *32*, e1902434. https://doi.org/10.1002/adma.201902434.

Wan, C., Cai, P., Guo, X., Wang, M., Matsuhisa, N., Yang, L., Lv, Z., Luo, Y., Loh, X.J., and Chen, X. (2020). An artificial sensory neuron with

visual-haptic fusion. Nat. Commun. *11*, 4602. https://doi.org/10.1038/s41467-020-18375-y.

Wang, Z., Rao, M., Han, J.W., Zhang, J., Lin, P., Li, Y., Li, C., Song, W., Asapu, S., Midya, R., et al. (2018). Capacitive neural network with neuro-transistors. Nat. Commun. *9*, 3208–3210. https://doi.org/10.1038/s41467-018-05677-5.

Wang, C.Y., Liang, S.J., Wang, S., Wang, P., Li, Z., Wang, Z., Gao, A., Pan, C., Liu, C., Liu, J., et al. (2020a). Gate-tunable van der Waals heterostructure for reconfigurable neural network vision sensor. Sci. Adv. *6*, eaba6173. https://doi.org/10.1126/sciadv. aba6173.

Wang, Z., Wu, H., Burr, G.W., Hwang, C.S., Wang, K.L., Xia, Q., and Yang, J.J. (2020b). Resistive switching materials for information processing. Nat. Rev. Mater. *5*, 173–195. https://doi.org/10.1038/s41578-019-0159-3.

Wang, Z., Li, C., Lin, P., Rao, M., Nie, Y., Song, W., Qiu, Q., Li, Y., Yan, P., Strachan, J.P., et al. (2019). In situ training of feed-forward and recurrent convolutional memristor networks. Nat. Mach. Intell. *1*, 434–442. https://doi.org/10.1038/s42256-019-0089-1.

Wu, C., Kim, T.W., Guo, T., Li, F., Lee, D.U., and Yang, J.J. (2016). Mimicking classical conditioning based on a single flexible memristor. Adv. Mater. *29*, 1602890. https://doi.org/10.1002/adma.201602890.

Yan, B., Kuang, D., Wang, W., Wang, Y., Sun, B., and Zhou, G. (2022). Investigation of multi-photoconductance state induced by light-sensitive defect in TiOx-based memristor. Appl. Phys. Lett. *120*, 253506. https://doi.org/10.1063/5.0097106.

Yang, L., Zeng, Z., and Wen, S. (2018). A full-function Pavlov associative memory implementation with memristance changing circuit. Neurocomputing *272*, 513–519. https://doi.org/10.1016/j.neucom.2017.07.020.

Zhang, Z., Wang, S., Liu, C., Xie, R., Hu, W., and Zhou, P. (2020). All-in-one two-dimensional retinomorphic hardware device for motion detection and recognition. Nat. Nanotechnol. *17*, 27–32. https://doi.org/10.1038/s41565-021-01003-1.

Zhang, Y., and Zeng, Z. (2021). A multi-functional memristive pavlov associative memory circuit based on neural mechanisms. IEEE Trans. Biomed. Circ. Syst. *15*, 978–993. https://doi.org/10.1109/TBCAS.2021.3108354.

Zhou, G., Duan, S., Li, P., Sun, B., Wu, B., Yao, Y., Yang, X., Han, J., Wu, J., Wang, G., et al. (2018). Coexistence of negative differential resistance and resistive switching memory at room temperature in TiOx modulated by moisture. Adv. Electron. Mater. *4*, 1700567. https://doi.org/10.1002/aelm.201700567.

Zhou, F., Zhou, Z., Chen, J., Choy, T.H., Wang, J., Zhang, N., Lin, Z., Yu, S., Kang, J., Wong, H.S.P., and Chai, Y. (2019a). Optoelectronic resistive random-access memory for neuromorphic vision sensors. Nat. Nanotechnol. *14*, 776–782. https://doi.org/10.1038/s41565-019-0501-3.

Zhou, G., Ren, Z., Wang, L., Sun, B., Duan, S., and Song, Q. (2019b). Artificial and wearable albumen protein memristor arrays with integrated memory logic gate functionality. Mater. Horiz. *6*, 1877–1882. https://doi.org/10.1039/C9MH00468H.

Zhou, G., Ren, Z., Wang, L., Wu, J., Sun, B., Zhou, A., Zhang, G., Zheng, S., Duan, S., and Song, Q. (2019c). Resistive switching memory integrated with amorphous carbon-based nanogenerators for self-powered device. Nano Energy *63*, 103793. https://doi.org/10.1016/j.nanoen.2019.05.079.

Zhou, G., Yang, X., Xiao, L., Sun, B., and Zhou, A. (2019d). Investigation of a submerging redox behavior in Fe2O3 solid electrolyte for resistive switching memory. Appl. Phys. Lett. *114*, 163506. https://doi.org/10.1063/1.5089147.

Zhou, G., Ren, Z., Sun, B., Wu, J., Zou, Z., Zheng, S., Wang, L., Duan, S., and Song, Q. (2020). Capacitive effect: an original of the resistive switching memory. Nano Energy *68*, 104386. https://doi.org/10.1016/j.nanoen.2019.104386.

Zhou, G., Sun, B., Hu, X., Sun, L., Zou, Z., Xiao, B., Qiu, W., Wu, B., Li, J., Han, J., et al. (2021). Negative photoconductance effect: an extension function of the TiOx-Based memristor. Adv. Sci. *8*, 2003765–2005383. https://doi.org/10.1002/advs.202003765.

Zhou, G., Wang, Z., Sun, B., Zhou, F., Sun, L., Zhao, H., Hu, X., Peng, X., Yan, J., Wang, H., et al. (2022). Volatile and nonvolatile memristive devices for neuromorphic computing. Adv. Electron. Mater. *8*, 2101127. https://doi.org/10.1002/aelm.202101127.

Ziegler, M., Soni, R., Patelczyk, T., Ignatov, M., Bartsch, T., Meuffels, P., and Kohlstedt, H. (2012). An electronic version of Pavlov's dog. Adv. Funct. Mater. *22*, 2744–2749. https://doi.org/10.1002/adfm.201200244.

STAR★METHODS

KEY RESOURCES TABLE

REAGENT or RESOURCE	SOURCE	IDENDIFIER
Chemicals, peptides, and recombinant proteins		
Ethanol (>99.9%, GC)	Aladdin	CAS: 64-17-5
Metal steel sheet (Fe-C alloy)	Kobetool	N/A
Ag target (>99.99%, 4N)	Beijin Jinyuan Adv. Mater. Technol.	N/A

RESOURCE AVAILABILITY

Lead contact

Further information and requests for resources and reagents should be directed to and will be fulfilled by the lead contact, Prof. Guangdong Zhou (zhougd@swu.edu.cn).

Materials availability

All materials generated in this study are available from the lead contact.

Data and code availability

This study does not generate data sets/code.

EXPERIMENTAL MODEL AND SUBJECT DETAILS

This study does not use experimental models typical in the life sciences.

METHOD DETAILS

All measurements of the electric properties were carried out in the air atmosphere. The Ag electrodes were deposited by the magnetron sputtering. Analytically pure chemical was used without further purification. The deionized water with the resistance of 18 MΩ. The measurements, instruments, device fabrication and characterization, and circuit simulation are listed as follows.

Measurements and instruments

The morphology and cross-section structure of the FeO_x film were characterized by the field emission scanning electron microscopy (FE-SEM, JSM-6510). The crystal structure was measured by the high-resolution transmission electron microscopy (HR-TEM, JEM-2100F) and X-ray diffraction (XRD-7000). The current-voltage curves (*I-V*) and current-time curves (*i-t*) are measured by the electrochemical workstation (CHI, 760E). The software of PSpice (Cadence 17.2 Pspice) is used to conduct the circuit simulations.

Device fabrication and characterization

A 2 × 2 cm2 Fe-C alloy sheet was orderly cleaned by the deionized water, ethanol, and deionized water at 60°C for 45 minutes. The cleaned Fe-C alloy sheet was dried at 85°C in N_2 for 3 hours. Air plasma cleaner (PDC-32G-2) was employed to clean the surface of the dried Fe-C alloy sheet for 90 seconds in order to remove the possible contaminants. The processed Fe-C alloy sheet was transferred into a glove-box to control the moisture air with a relative humidity of 85%. After reacting with oxygen and water for 72 hours, the FeO_x switching layer was synthesized.

Ag target with a purity of 99.99% was employed to deposit Ag top electrode. The Ag electrode with a diameter of 200 μm and ~50 nm thickness was sputtered at 20 W in 0.85 Pa Ar for 30 seconds. Thus, the memristor with the structure of Ag/FeO_x/Fe-C alloy sheet was developed. The self-designed glovebox was employed to control the relative humidity.

Circuit model and soft simulation

Classical Pavlov conditioning can be divided into three phases, i.e., the premise phase, 1st learning phase and 1st forgetting phase. Notably, the control voltage g and light signal SL remain in low-level state VL.

The premise phase:

When meat signal $S_M = V_H$ and ring signal $S_R = V_L$, the node voltage equation according to Kirchhoff's current law (KCL) is expressed as:

$$\frac{V_H - V_S}{R_1} + \frac{V_H - V_S}{M_1} = 0 \quad \text{(Equation 10)}$$

According to the parameter setting, the initial memristance of M_1 is R_H. As $R_1 << R_H$, (Equation 10) is simplified to $V_S = V_H$. At this point, output voltage $V_{out1} = V_{dd}$, indicating that the dog secretes saliva.

When $S_M = V_L$ and $S_R = V_H$, the node voltage equation according to KCL is described as:

$$\frac{V_L - V_S}{R_1} + \frac{V_H - V_S}{M_1} = 0 \quad \text{(Equation 11)}$$

Based on the parameter setting, the initial memristance of M_1 is R_H. Due to $R_1 << R_H$, (Equation 11) can be further simplified to $V_S = V_L$. Output voltage V_{out1} = Gnd, indicating that the dog dose not secrete saliva.

1st learning phase: When $S_M = S_R = V_H$, the node voltage equation according to KCL is:

$$\frac{V_H - V_S}{R_1} + \frac{V_L - V_S}{M_1} = 0 \quad \text{(Equation 12)}$$

According to the law of change of memristance, M_1 quickly switch from BLC state to RS state and the output $V_{out}=V_{dd}=V_H$, which means that the dog secretes saliva.

1st forgetting phase: When $S_M = V_L$ and $S_R = V_H$, the node voltage equation can be obtained according to KCL as:

$$\frac{V_L - V_S}{R_1} + \frac{V_H - V_S}{M_1} = 0 \quad \text{(Equation 13)}$$

Notably, once the meat signal S_M is removed, the 1st forgetting phase will start along with the entire secondary Pavlov conditioned reflex.

Similarly, the secondary Pavlov conditioned reflex can also be divided into three phases, i.e., the premise phase, 2nd learning phase and 2nd forgetting phase. Notably, the control signal g always keeps in V_H, while the meat signal always keeps in V_L (i.e., the meat is removed).

The premise phase:

When ring signal $S_R = V_H$ and light signal $S_L = V_L$, the node voltage equation according to Kirchhoff's current law (KCL) is expressed as:

$$\frac{V_H - V_S}{R_2} + \frac{V_H - V_S}{M_2} = 0 \quad \text{(Equation 14)}$$

According to the parameter setting, the initial memristance of M_2 is R_H. As $R_2 << R_H$, (Equation 14) is simplified to $V_S = V_H$. At this point, output voltage $V_{out2} = V_{dd}$, indicating that the dog secretes saliva.

When $S_R = V_L$ and $S_L = V_H$, the node voltage equation according to KCL is described as:

$$\frac{V_L - V_S}{R_2} + \frac{V_H - V_S}{M_2} = 0 \quad \text{(Equation 15)}$$

Based on the parameter setting, the initial memristance of M_2 is R_H. Due to $R_2 << R_H$, (6) can be further simplified to $V_S = V_L$. Output voltage V_{out2} = Gnd, indicating that the dog dose not secrete saliva.

2nd learning phase: When $S_R = S_{RL} = V_H$, the node voltage equation according to KCL is:

$$\frac{V_H - V_S}{R_2} + \frac{V_L - V_S}{M_2} = 0 \qquad \text{(Equation 16)}$$

According to the law of change of memristance, M_1 increases while M_2 decreases in a certain time range. The output V_{out}=V_{dd}=V_H, which means that the dog secretes saliva and the associative memory between the ring and light is established.

2nd forgetting phase: When $S_R = V_L$ and $S_L = V_H$, the node voltage equation can be obtained according to KCL as:

$$\frac{V_L - V_S}{R_2} + \frac{V_H - V_S}{M_2} = 0 \qquad \text{(Equation 17)}$$

According to the law of change of memristance, M_1 remains unchanged while M_2 increases. The output V_{out} decreases from V_H to V_L, which means that the dog does not secrete saliva and the previously established secondary conditioned reflex is disappeared. Therefore, the circuit model can be established by the Equations 10–17.

QUANTIFICATION AND STATISTICAL ANALYSIS

This study does not include statistical analysis or quantification.

ADDITIONAL RESOURCES

Additional resource contains code programming for the memristor-based circuit model can be found in the supplemental information.